Quantitative Determination of Competitive Molecular Adsorption on Gold Nanoparticles Using Attenuated Total Reflectance–Fourier Transform Infrared Spectroscopy

De-Hao Tsai,[†] Melissa Davila-Morris,[†] Frank W. DelRio,[†] Suvajyoti Guha,[†,‡] Michael R. Zachariah,[†,‡] and Vincent A. Hackley*,[†]

[†]Material Measurement Laboratory, National Institute of Standards and Technology, Gaithersburg, Maryland 20899, United States

[‡]Departments of Mechanical Engineering and Chemistry, University of Maryland, College Park, Maryland 20740, United States

Ⓢ *Supporting Information*

ABSTRACT: Surface-sensitive quantitative studies of competitive molecular adsorption on nanoparticles were conducted using a modified attenuated total reflectance–Fourier transform infrared (ATR-FTIR) spectroscopy method. Adsorption isotherms for thiolated poly(ethylene glycol) (SH-PEG) on gold nanoparticles (AuNPs) as a function of molecular mass (1, 5, and 20 kDa) were characterized. We find that surface density of SH-PEG on AuNPs is inversely proportional to the

molecular mass (M_m). Equilibrium binding constants for SH-PEG, obtained using the Langmuir adsorption model, show the binding affinity for SH-PEG is proportional to M_m. Simultaneous competitive adsorption between mercaptopropionic acid (MPA) and 5 kDa SH-PEG (SH-PEG5K) was investigated, and we find that MPA concentration is the dominant factor influencing the surface density of both SH-PEG5K and MPA, whereas the concentration of SH-PEG5K affects only SH-PEG5K surface density. Electrospray differential mobility analysis (ES-DMA) was employed as an orthogonal characterization technique. ES-DMA results are consistent with the results obtained by ATR-FTIR, confirming our conclusions about the adsorption process in this system. Ligand displacement competitive adsorption, where the displacing molecular species is added after completion of the ligand surface binding, was also interrogated by ATR-FTIR. Results indicate that for SH-PEG increasing M_m yields greater stability on AuNPs when measured against displacement by bovine serum albumin (BSA) as a model serum protein. In addition, the binding affinity of BSA to AuNPs is inhibited for SH-PEG conjugated AuNPs, an effect that is enhanced at higher SH-PEG M_m values.
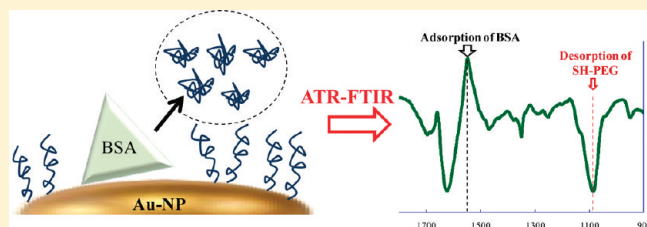
1. INTRODUCTION

The surface and interfacial properties of nanoscale particles, including effects associated with intentional or incidental molecular coatings, are known to have a dominant impact on their functionality, stability, transport, fate, and biological interactions.[1-8] In fact, surface engineering of nanoparticles is the principal method for obtaining desired functionalities for a wide range of applications in nanotechnology and bionanotechnology.[6,9-17] In many applications, nanoparticles essentially serve as carriers or platforms for delivering a payload to a specific location (i.e., passive or active targeting), and often the underlining particle is subordinate to the overlying surface coating with respect to its functionality and biological response.

An example is the use of functionalized nanoparticle-based vectors for targeted drug delivery, which remains one of the most promising applications of nanotechnology[11,16-19] with new drug therapies now entering the clinical testing pipeline.[20] Although the technical challenges of nanomedicine are substantial and nontrivial, particularly at the preclinical stage, the potential payoff is enormous and represents no less than a new paradigm for the way in which we diagnose and treat diseases such as cancer.[21-23] Using the nanoparticle vector's inherent surface chemistry as a substrate, a combination of targeting, imaging, and therapeutic functionalities can be attached. The benefits of this approach are manifold: targeting of cancer cells without damage to surrounding tissue, reduction or elimination of toxic side effects associated with standard chemotherapies, significant reduction in the required dose of expensive drugs, earlier and more precise detection, and improved imaging contrast to confirm successful targeting.[18] Despite these obvious benefits, technical challenges remain with respect to quantitatively characterizing the amount, location, conformation, and stability of surface-bound ligands on multifunctional nanoscale particles.

In our previous work, we have demonstrated that physical characterization methods can be used for the direct characterization of molecular conjugation on the surface of gold nanoparticles

(AuNPs).[14,16,17] The general concept is to measure the change in particle dimensions as ligand molecules attach to the surface. The molecular surface density can be quantified based on the change in the particle's physical size, accompanied by knowledge of the molecular chain length (i.e., the increase of particle size contributed by each ligand).[14,16,17] The major advantages of physical characterization methods include speed of analysis (e.g., minutes per measurement), high spatial resolution (down to 0.3 nm, depending on the approach), availability and affordability of required instrumentation, and, most importantly, transferability of the methodology for use in a routine nonclinical formulation design and manufacturing environment and to support regulatory requirements. For the purpose of method improvement, and specifically to verify the accuracy, it is important to have orthogonal comparisons to complement the physical characterization approach.[24]

The present investigation focuses on attenuated total reflectance–Fourier transform infrared (ATR-FTIR) spectroscopy, which has been used previously in a variety of applications.[24−27] The advantage of ATR-FTIR, relative to transmittance or diffuse-reflectance modes, is enhanced control of the IR beam path by utilizing the evanescent wave generated along the ATR element. This translates into an improved signal-to-noise ratio for the analysis of surface-bound molecular species and provides the capacity to conduct quantitative or semiquantitative analyses.[24,26,27] By incorporating a liquid flow cell, ATR-FTIR can be used to identify and characterize the quantity of molecules of interest presenting in the solution phase. Furthermore, by depositing a film of nanoparticles onto the ATR substrate, the relative quantity of molecules attached to particle surfaces in contact with the bulk solution and within the stable porous film can be characterized semiquantitatively. McQuillan et al.[28,29] studied the molecular interaction with sol–gel metal oxide films using ATR-FTIR. Because of the controlled beam path, and the extent of adsorption involved in those studies, the isoelectric point, relative surface coverage, and equilibrium binding constants were characterized based on adsorption isotherm data. Li et al.[25] applied ATR-FTIR to study the interactions of small molecules in solution trapped within a polymer membrane. The ligand concentrations retained in the membrane were characterized quantitatively, providing the capacity to study environmental contaminants.

Our principal objective here was to develop methods based on ATR-FTIR used in conjunction with a liquid flow cell to quantify the adsorption, equilibrium binding constants, and surface density for thiolated poly(ethylene glycol) (SH-PEG) on citrate-stabilized AuNPs. On the basis of the corresponding surface density, we can estimate the surface conformation of SH-PEG. For orthogonal comparison, electrospray differential mobility analysis (ES-DMA), a high-resolution physical characterization method, was utilized to estimate surface density and binding affinity for SH-PEG on AuNPs.

In addition, we sought to apply these methods to interrogate the competitive adsorption kinetics for SH-PEG in the presence of other relevant molecular species. Two types of competitive adsorption were investigated in this study: simultaneous competitive adsorption and ligand displacement competitive adsorption.

During the formation of SH-PEG-functionalized AuNP products for therapeutic applications, other additives or presenting impurities may compete for adsorption sites on the surface of AuNPs. Hence it is necessary to interrogate the competitive adsorption process between multiple components adsorbing to the AuNP surface and to develop effective methods to characterize this process both qualitatively and quantitatively. In a previous study, we used physical measurement approaches to characterize the competitive adsorption between SH-PEG and mercaptoproprionic acid (MPA), and as a result, we were able to successfully quantify the surface density of SH-PEG and to determine binding affinity.[17] Although physical characterization methods demonstrate a substantial capacity to characterize molecular conjugation on nanoparticles with high speed and resolution,[15−17] an obvious capability gap is that particle size is the only experimental output and thus subject to interference from other mechanisms that may induce changes in particle size. Moreover, it is difficult to differentiate between different ligands coexisting on the AuNP surface, unless they exhibit a considerable molecular size differential. Thus, for the study of competitive adsorption between different ligands, it is a challenge to distinguish the extent of relative adsorption due to the difficulty in differentiating each contribution to the overall increase of particle size. Finally, for nanoparticles that have a broad size distribution, it is difficult, if not impossible, to determine if an observed increase in particle size is due to molecular conjugation or to particle agglomeration, while the resolution with respect to quantifying size change is negatively impacted. On the other hand, ATR-FTIR offers an effective approach to differentiate competitive adsorption between different, even similarly sized, ligands on the surface of AuNPs and can be potentially used to benchmark physical-based measurements.

Equally relevant for therapeutic applications is the so-called ligand displacement competitive adsorption scenario, where the displacing ligand interacts subsequent to formation of the target ligand–AuNP conjugate. Whereas simultaneous competitive adsorption reflects both differences in affinity (leading to displacement of adsorbed ligands) as well as diffusional effects (e.g., smaller molecules diffuse to the reactive AuNP surface faster relative to larger molecules), ligand displacement is primarily driven by affinity differences with a secondary contribution possibly due to steric hindrance effects. For instance, after SH-PEG-functionalized AuNPs are delivered into a complex biological matrix, other potential ligands will present themselves, including the ubiquitous serum albumin protein. At physiological pH, albumins, irrespective of species specificity, generally present a single external thiol available for conjugation to the AuNP surface.[24] For ligand displacement, we selected bovine serum albumin (BSA) as a representative serum protein to investigate the stability of PEG-conjugated AuNPs once they enter the mammalian circulatory system.

2. EXPERIMENTAL SECTION

a. Materials and Chemicals. Nominal 60 nm citrate-stabilized AuNPs were obtained from Ted Pella Inc. (Redding, CA).[30] The number concentration of AuNPs in the native solution is estimated to be 2.6×10^{10} cm^{-3}. SH-PEG (1 and 20 kDa) were obtained from Nanocs (New York, NY), and 5 kDa SH-PEG was obtained from JenKem Technology USA (Allen, TX). SH-PEG was used at concentrations ranging from 2.8×10^{-4} to 20 mmol/L. Reagent grade (≥98% protein, ≤3 endotoxin unit/mg, fatty acid- and IgG-free) BSA was obtained from SeraCare Life Science (Milford, MA) and was utilized at concentrations ranging from 7.5×10^{-4} to 0.30 mmol/L. Aqueous MPA (99+%) and ammonium acetate (99.9%) were obtained from Sigma-Aldrich (St. Louis, MO). MPA solutions were prepared in the concentration
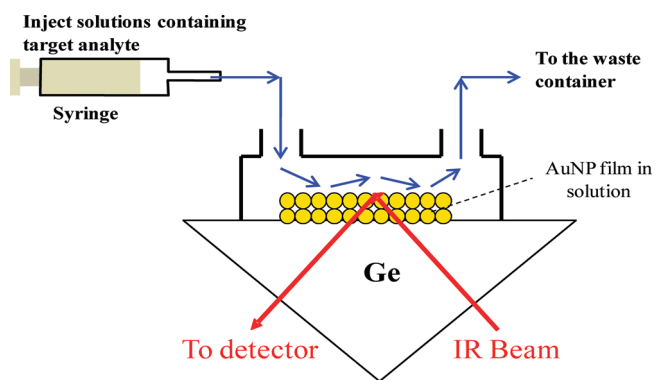
Figure 1. Schematic of the ATR-FTIR equipped with a Ge flat and liquid flow cell.

range from 0 to 1.44 mmol/L, while aqueous 2—4 mmol/L ammonium acetate solutions were prepared to adjust the ionic strength for ES-DMA analysis. Biological grade 18.2 M$\Omega\cdot$cm deionized (DI) water (Aqua Solutions, Jasper, GA) was used for preparing all solutions and diluted AuNP suspensions.

b. Flow Cell ATR-FTIR System. ATR-FTIR spectroscopy was performed using a Nicolet Spectra 750 FTIR spectrometer equipped with a Thunder Dome Germanium ATR accessory (Thermo Scientific, Madison, WI). A schematic diagram of the ATR-FTIR setup is shown in Figure 1. Spectra were collected from 128 scans with a resolution of 1 cm^{-1}. For sample preparation, 200 and 800 μL of native AuNP solution were first concentrated to between 8 and 20 μL (i.e., at least 10×) by centrifugation and then drop-cast onto the surface of the clean germanium ATR crystal. After evaporating the solvent in a clean bench at room temperature, a AuNP film was formed on the crystal surface. Then, a flow cell unit (Thermo Scientific) was attached to the top of the ATR crystal in order to allow fluid to contact and penetrate the AuNP film. Background spectra were recorded by introducing DI water into the flow cell. Solutions with various concentrations of molecular adsorbates were then introduced into the flow cell, and the resulting spectra were recorded. The experiments were performed at ≈21 °C using a sequential injection measurement: sample solutions containing selected ligands were injected sequentially into the flow cell ranging from low to high concentration. For the analysis of ligand displacement competitive adsorption, the background spectrum subtracted from the experimental runs was obtained in DI water, but after the target ligand was initially adsorbed to the AuNP film; this procedure results in negative absorbance for the characteristic IR band of the target ligand if the ligand is displaced from the AuNP surface.

Because the IR beam path is controlled, providing a constant control volume, V_T, we can calibrate the measured IR absorbance, I_{ab}, against the known concentration of unbound molecules, C_m. Assuming the IR absorption coefficients of molecules are unchanged upon adsorbing onto AuNPs, the concentration of molecules presenting in V_T can be quantified. On the basis of the Beer—Lambert law,[31] a linear correlation is expected between I_{ab} and C_m

$$I_{ab} = (k_{ab}l)C_m = k_{ab}^* C_m \qquad (1)$$

where k_{ab} is absorption cross section, l is the path length of the IR beam, and k_{ab}^* is absorption coefficient ($= k_{ab}l$). For simplifying the analysis without reducing accuracy, I_{ab} is determined by the measured heights of the absorption peaks.

In order to quantify the molecular surface density on AuNPs, σ, we need to determine (1) N_m, the quantity of molecules presenting in V_T, and (2) A_{film}, the surface area of the AuNP film on the Ge crystal surface. Details of determining V_T and A_{film} are described in section 1 of the

Supporting Information. Based on the IR absorbance, molecular surface density can then be calculated using the relationship

$$\sigma = \frac{N_m}{A_{film}} = \frac{V_T}{A_{film}} \frac{I_{ab}}{k_{ab}^*} \qquad (2)$$

c. Electrospray Differential Mobility Analysis (ES-DMA). The ES-DMA system consists of an electrospray aerosol generator (Model 3480, TSI Inc., Shoreview, MN), a differential mobility analyzer (DMA, Model 3080n, TSI Inc.), and a condensation particle counter (CPC, Model 3025, TSI Inc.). Details of the ES-DMA experimental setup have been described in previous publications[14,16,17,19] and are also summarized in section 2 of the Supporting Information.

d. Measurement Uncertainty. Error bars shown in figures and uncertainty ranges associated with measurement values represent one standard deviation calculated from replicate (2—4) measurements performed under repeatability conditions.

3. RESULTS AND DISCUSSION

a. Quantification of Unbound Molecules in Solution Using ATR-FTIR. In order to correlate IR absorbance to the quantity of molecules presenting in the control volume (eq 1) and also to examine the capacity for quantification for ATR-FTIR results, we first characterize the concentration of unbound molecules in solution (i.e., without AuNPs present). Figure 2a shows representative IR spectra obtained for unbound MPA and SH-PEG with three different molecular mass, M_m, values (denoted as SH-PEG1K, SH-PEG5K, and SH-PEG20K for M_m = 1, 5, and 20 kDa, respectively). For SH-PEG, a strong absorption band was observed near 1080 cm^{-1}, representing the C—O stretching of the ethylene glycol monomers.[16,32] For MPA, a significant absorbance is observed near 1230—1260 cm^{-1}, representing the C—O stretching of the carboxylic group in MPA.[16,32] In order to optimize sensitivity, the peaks at 1080 cm^{-1} for SH-PEG and 1240 cm^{-1} for MPA were chosen for quantitative analysis (denoted as (C—O)$_{PEG}$ and (C—O)$_{MPA}$ in the following text).

Figure 2b shows measured calibration curves for molecular concentration versus the corresponding IR absorbance. A clear linear relation of I_{ab} versus C_m was found for all four target ligands characterized. The results demonstrate consistency with eq 1, confirming a strong capacity for ATR-FTIR quantitative analysis. k_{ab}^* was then obtained from the slopes of the regression fits. Comparing results obtained for SH-PEG as a function of M_m we found $k_{ab}^* \sim M_m$, indicating the molecular IR absorptivity is directly proportional to the number of repeating units per molecular chain regardless of the final form of the chains (i.e., M_m of polymer). In the next section we will use eq 2 with the corresponding k_{ab}^* values to quantify the uptake of ligands on the AuNP surface.

b. Characterization of Molecular Adsorption on AuNPs and Quantification of Surface Density. Having established that ATR-FTIR has the capacity for quantitative analysis, we apply the methodology to study molecular adsorption on AuNPs. Figure 3a—c shows the IR spectra of SH-PEG1K, SH-PEG5K, and SH-PEG20K in the presence of the AuNP film (produced using 800 μL of native AuNP suspension). Similar to the results for unbound SH-PEG (Figure 2), we observe a strong absorbance at 1080 cm^{-1} (i.e., C—O stretching of the ethylene glycol monomers) for all three SH-PEG following interaction with the AuNP film, and the intensity of (C—O)$_{PEG}$ increases significantly with the increase in SH-PEG concentration (C_{SH-PEG}). In addition to (C—O)$_{PEG}$, we observe
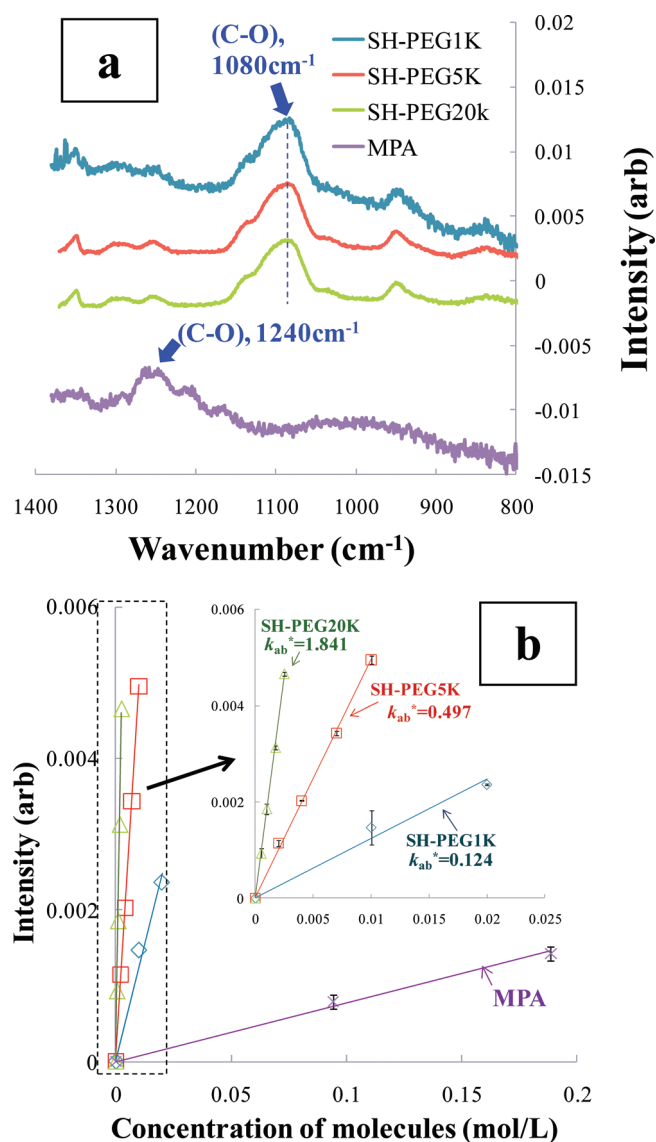
Figure 2. Quantitative analysis of free ligand concentration in DI water using ATR-FTIR. (a) IR spectra of unbound ligands in water. From top to bottom: SH-PEG1K, SH-PEG5K, SH-PEG20K, and MPA. The ligand mass fraction is 2% for all spectra. (b) I_{ab} vs C_m for SH-PEG1K (diamonds), SH-PEG5K (squares), SH-PEG20K (triangles), and MPA (crosses). Data are fit using linear regression with a slope k_{ab}^*.

a peak at 1400 cm^{-1} when the concentration of SH-PEG20K ($C_{SH\text{-}PEG20K}$) is higher than 0.005 mmol/L; for a discussion of this peak, please refer to section 3 of the Supporting Information.

Comparing the measured absorbance intensities, we observe that the intensity of the $(C-O)_{PEG}$ peak for (SH-PEG +AuNP) is significantly higher ($\approx 100\times$) relative to that of unbound SH-PEG at the same total concentration. This is due to the enriched SH-PEG concentration in the control volume as a result of adsorption within the AuNP film. By comparison, the contribution from unbound molecules in water is essentially negligible. To confirm this statement experimentally, after removing any unbound SH-PEG from the system by flushing with DI water (denoted as "water cleaned" in Figure 3a−c), there is no significant decrease in $(C-O)_{PEG}$ intensity. This confirms that absorbance signals from $(C-O)_{PEG}$ are principally arising from

the SH-PEG−AuNP conjugate, and an increase in intensity for $(C-O)_{PEG}$ can therefore be attributed to an increase in SH-PEG attached to the AuNP surface within the deposited film.

Using the maximum measured I_{ab} from Figure 3a−c, the maximum surface density of SH-PEG, $\sigma_{SH\text{-}PEG,max}$, is obtained. However, the calculated $\sigma_{SH\text{-}PEG,max}$ is dependent on the quantity of AuNP suspension used to form the deposited film: $\sigma_{SH\text{-}PEG,max}$ increases $3\times$ when the volume of AuNP suspension used increases from 200 to 800 μL (equivalent to a $4\times$ increase in film thickness). The origin of this dependency is unclear, although there are several possibilities, including variation of the absorption coefficient within the AuNP film and nonuniformity of the deposited film (see Figure S2 and associated discussion based on AFM measurements in section 4 of the Supporting Information). To resolve this issue, we employed MPA as a calibrant; MPA is a well-studied short chain ligand widely used to form self-assembled monolayers on Au surfaces and has a maximum surface density of ≈ 6.5 nm^{-2}.[33] From the IR spectra (Figure 3d), we observe a strong absorbance of $(C-O)_{MPA}$ after introducing MPA to the AuNP film at two different film thicknesses (i.e., based on different volumes of AuNP suspension). Using eq 2 to calculate the maximum surface density for MPA, $\sigma_{MPA,max}$, the results indicate that a film produced from 200 μL of AuNP suspension (denoted as condition I) yields a value of $\sigma_{MPA,max} \approx 10$ nm^{-2}, whereas a film produced from 800 μL of AuNP suspension (denoted as condition II) yields a value of $\sigma_{MPA,max} \approx 29$ nm^{-2}. The implication is condition I shows better accuracy in the measurement of surface density, while condition II provides better sensitivity in detection of the occurrence of molecular adsorption at low surface density values. To improve the accuracy, we scaled the results by using the surface density of MPA for different film thicknesses

$$\sigma_{SH\text{-}PEG} = \sigma_{MPA,0}\frac{N_{SH\text{-}PEG}}{N_{MPA}} = \sigma_{MPA,0}\frac{I_{ab,SH-PEG}k_{ab,MPA}^*}{I_{ab,MPA}k_{ab,SH-PEG}^*} \quad (3)$$

where $\sigma_{SH\text{-}PEG}$ is the surface density of SH-PEG and $\sigma_{MPA,0}$ is the reference reported maximum surface density of MPA.[33] N_{MPA} and $N_{SH\text{-}PEG}$, $I_{ab,MPA}$ and $I_{ab,SH\text{-}PEG}$, and $k_{ab,MPA}$ and $k_{ab,SH\text{-}PEG}$ are the N_m, I_{ab}, and k_{ab}^* of MPA and SH-PEG at the same film thickness, respectively.

Next we investigate the effect of M_m on $\sigma_{SH\text{-}PEG,max}$ using eq 3. As shown in Figure 3e, $\sigma_{SH\text{-}PEG,max}$ is approximately inversely proportional to M_m ($\sigma_{SH\text{-}PEG,max} \sim M_m^{-1.1}$). The result is close to the observation by Netz et al. ($\sigma_{max} \sim M_m^{-1.07}$, where σ_{max} is the maximum surface density of polymers), indicating $\sigma_{SH\text{-}PEG,max}$ is dominated by the random walk radius, $\langle x^2 \rangle^{0.5}$, of SH-PEG.[34] In our previous study, we observed that the conformation of SH-PEG can be transformed from random-walk coil to a more brushlike chain with an increase in surface density. When approaching the maximum surface density for a self-assembled layer (e.g., $\sigma_{MPA,max}$), the ligand may behave more like a vertically aligned brush with confined motion on the surface of the particle. As shown in Figure 3e, $\sigma_{SH\text{-}PEG,max}$ for the three M_m values used in this study, is at least $3\times$ less than the corresponding $\sigma_{MPA,max}$. Hence, it is reasonable to assume that although the PEG chain may behave as a brush near the particle surface, the outer portion of the SH-PEG chains may still follow a random-walk motion even near maximum surface density.

c. Adsorption Isotherms and Quantification of Binding Affinity for SH-PEG on AuNPs. In the previous section, we have demonstrated proof of principle for application of ATR-FTIR in
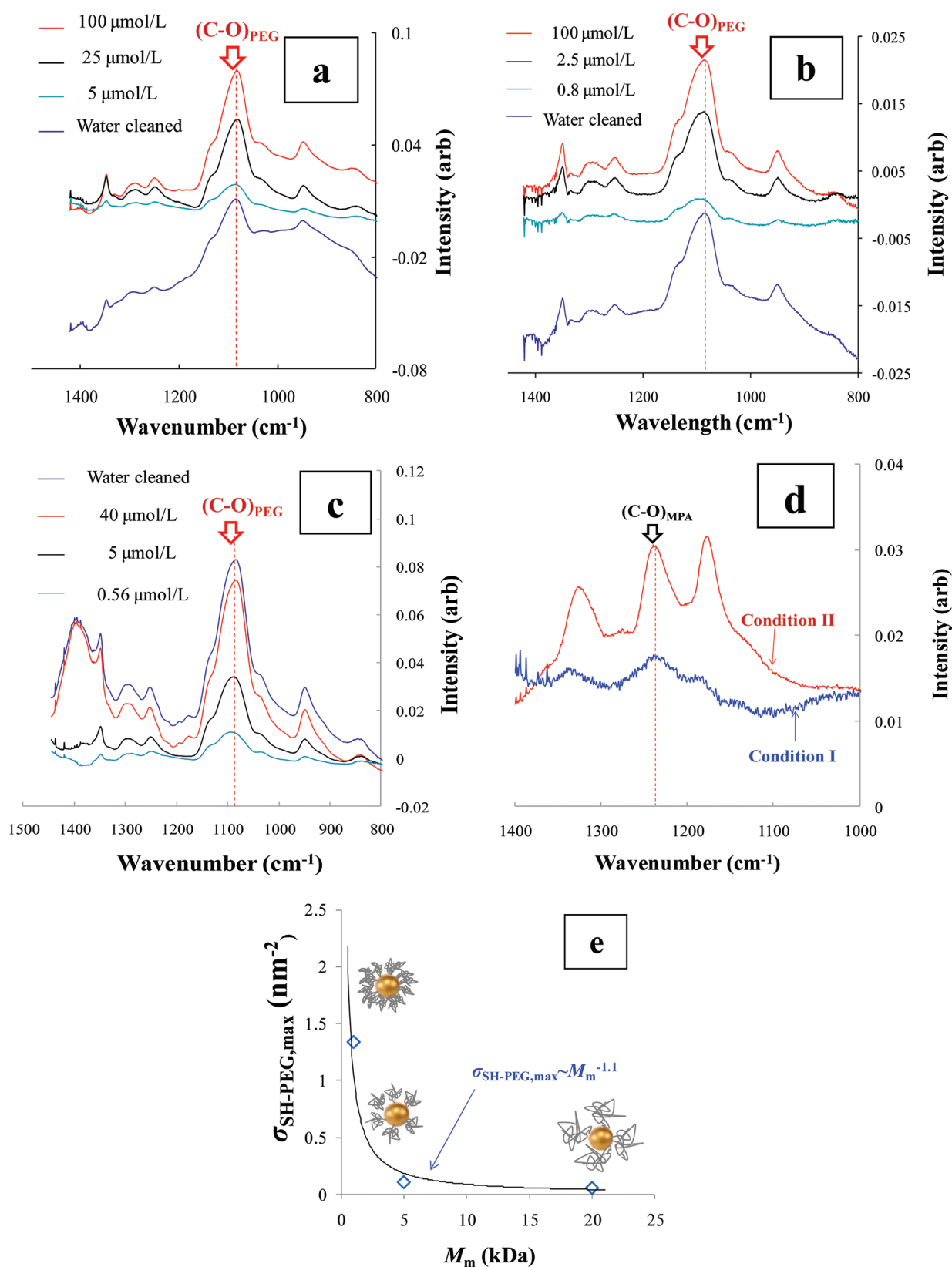
Figure 3. Characterization of molecular adsorption on AuNPs using ATR-FTIR. (a) IR spectra for SH-PEG1K with AuNPs. (b) IR spectra for SH-PEG5K with AuNPs. (c) IR spectra for SH-PEG20K with AuNPs. A suspension volume of $800\,\mu$L (condition II) was used for forming AuNP films used in (a)−(c). (d) IR spectra for (MPA + AuNPs) comparing condition I ($200\,\mu$L of AuNP suspension) and condition II. $C_{MPA} = 943\,\mu$mol/L. (e) Effect of molecular mass on the maximum surface density of SH-PEG calculated using eq 3. The water cleaned trace relates to a concentration of $1000\,\mu$mol/L for SH-PEG1K, $943\,\mu$mol/L for MPA, and $400\,\mu$mol/L for both SH-PEG5K and SH-PEG20K.
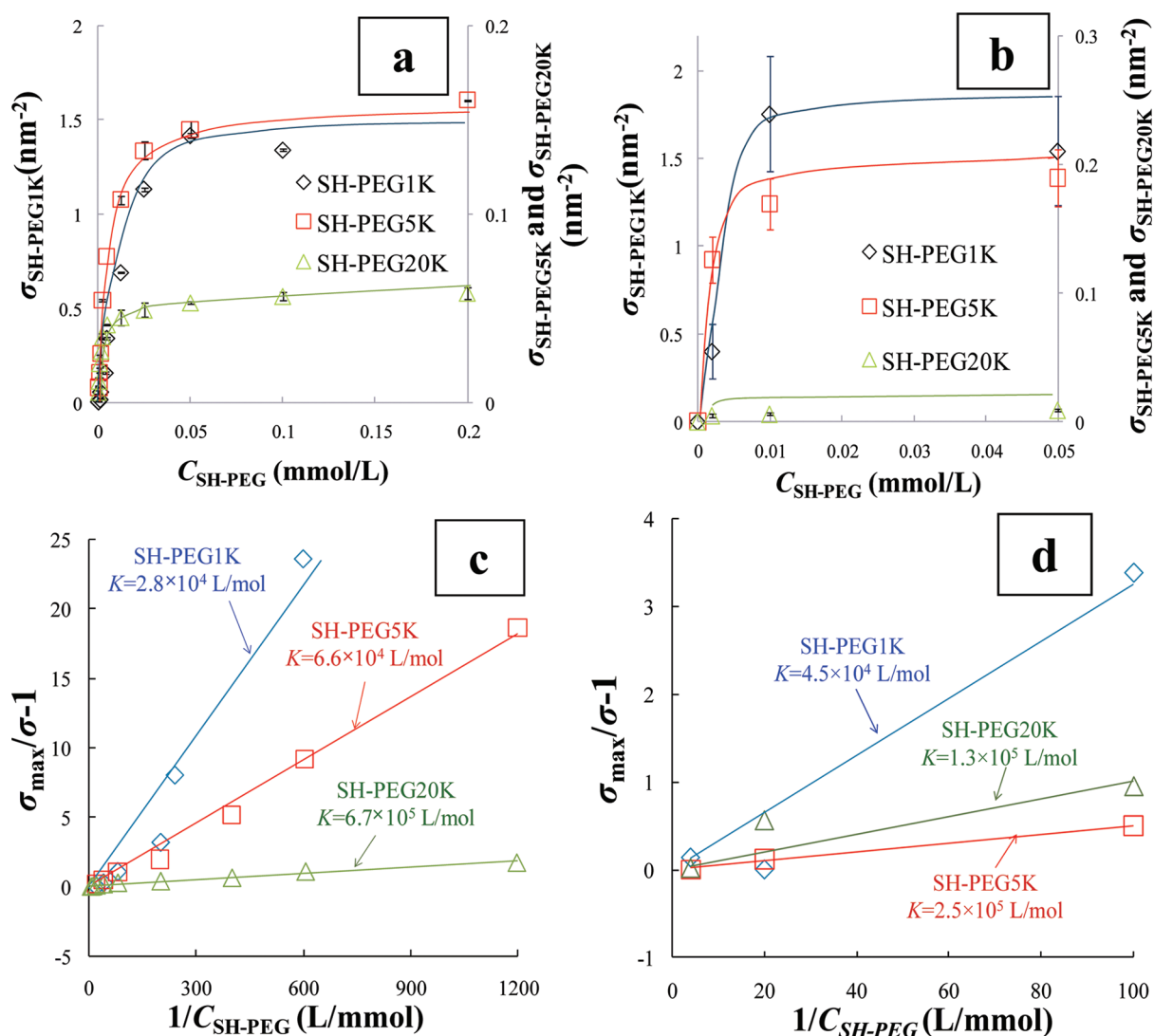
Figure 4. Adsorption isotherms for SH-PEG on AuNPs using ATR-FTIR and ES-DMA. (a) Adsorption isotherm curves obtained by ATR-FTIR. (b) Adsorption isotherms curves obtained by ES-DMA. Lines in (a) and (b) are to guide the eyes. (c) Fit to Langmuir equation for (a). (d) Fit to Langmuir equation for (b). Lines in (c) and (d) are linear fits of data using eq 5 with slopes of $1/K$, where K is the equilibrium binding constant for SH-PEG to the AuNP surface. Isotherms were determined at 21 °C.

Table 1. Summary of Adsorption Isotherm Results for SH-PEG on AuNPs Measured by ATR-FTIR and ES-DMA[a]

species	σ_{max} by IR (nm^{-2})	C_{max} by IR (mmol/L)	K by IR (L/mol)	σ_{max} by DMA (nm^{-2})	C_{max} by DMA (mmol/L)	K by DMA (L/mol)
SH-PEG1K	1.4	0.05	2.8×10^4	1.7	<0.03	4.5×10^4
SH-PEG5K	0.16	0.025	6.6×10^4	0.18	<0.03	2.5×10^5
SH-PEG20K	0.05	0.005	6.7×10^5	0.009	<0.03	1.3×10^5

[a] C_{max} is the required concentration for reaching saturation surface density (i.e., plateau adsorption).

the quantitative characterization of molecular adsorption on AuNPs. We now extend that methodology to determine adsorption isotherms for SH-PEG on AuNPs. Figure 4a shows σ_{SH-PEG} versus C_{SH-PEG} for three different chain lengths of SH-PEG, based on the results of Figure 3a−c. For the different M_m values, increasing C_{SH-PEG} increases σ_{SH-PEG} up to and approaching characteristic plateau values (as summarized in Table 1). We observe that the general tendency is for the plateau level and the associated minimum bulk concentration required to reach the plateau is inversely proportional to M_m.

For an orthogonal comparison, we employ ES-DMA, which has been used previously to study polymer adsorption on AuNPs.[14,17] From the increase in the cross-sectional area of particles as determined by ES-DMA, σ_{SH-PEG} can be calculated following adsorption of SH-PEG. We employ a previously developed analytical model[14,17]

$$\sigma_{SH-PEG} = \frac{[(d_{p,m} + \Delta d_{p,m})^2 - d_{p,m}{}^2]^2}{(2d_{p,m}\langle x^2 \rangle)^2} \quad (4)$$
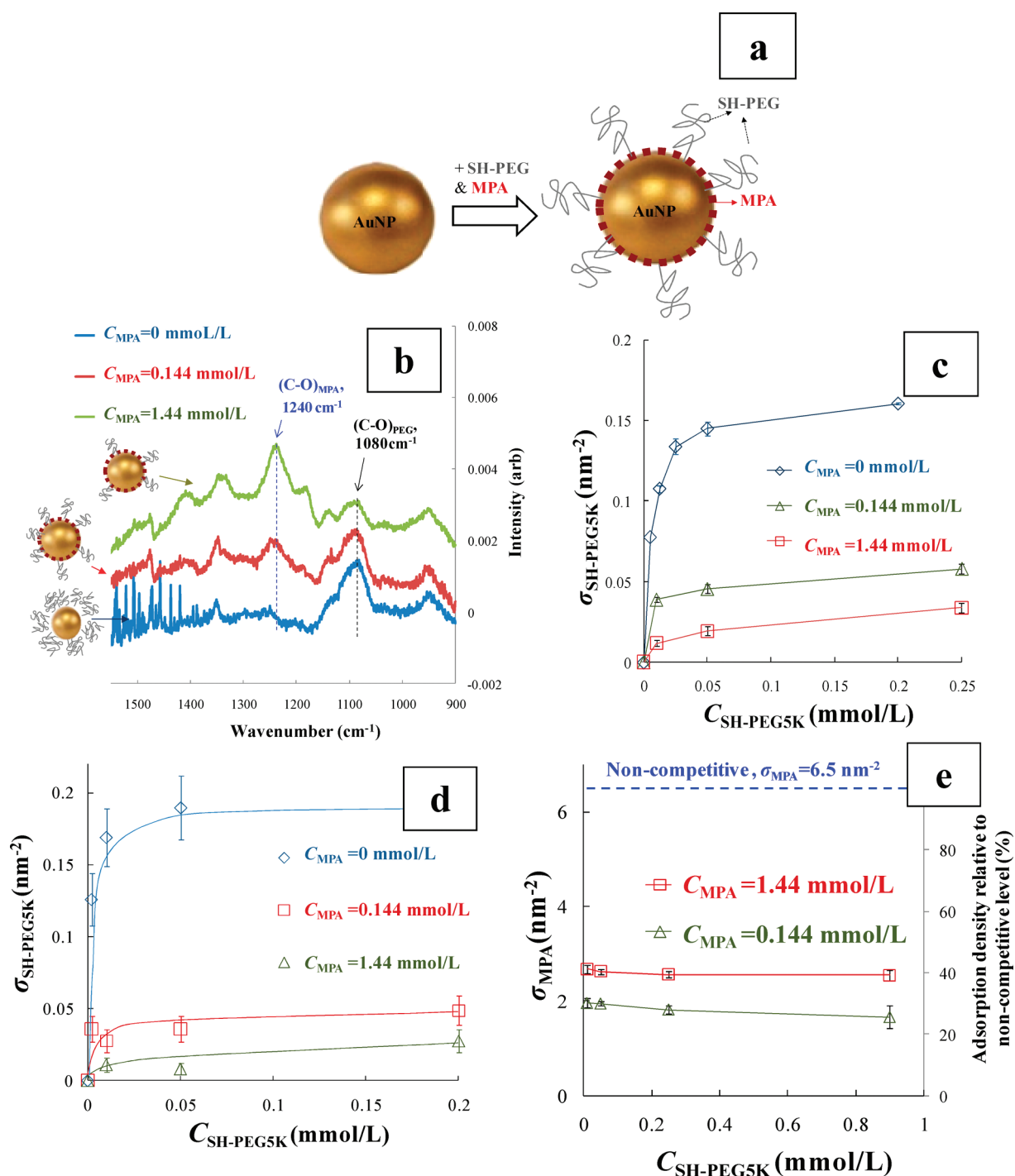
Figure 5. Simultaneous competitive adsorption of SH-PEG5K and MPA on AuNPs. (a) Cartoon depiction of (SH-PEG5K + MPA) adsorbing to AuNPs. (b) IR spectra of molecular conjugates (SH-PEG5K + MPA) as a function of C_{MPA}. $C_{SH-PEG5K}$ was fixed at 0.05 mmol/L. (c) Adsorption isotherms for SH-PEG5K in the presence of MPA determined by ATR-FTIR. (d) Adsorption isotherms for SH-PEG5K in the presence of MPA measured by ES-DMA. (e) Adsorption isotherms for MPA in the presence of SH-PEG5K determined by ATR-FTIR. Lines are to guide the eyes.

where $d_{p,m}$ is the average mobility diameter of the native AuNPs and $\Delta d_{p,m}$ is the increase in particle size following adsorption. For freely jointed Gaussian chains, the random-walk radius of SH-PEG, $\langle x^2 \rangle^{0.5}$, is estimated to be 1.6, 3.7, and 7.3 nm for SH-PEG1K, SH-PEG5K, and SH-PEG20K, respectively.[17]

Figure 4b shows adsorption isotherms measured obtained by ES-DMA. The results are similar and consistent with results shown previously for ATR-FTIR (as summarized in Table 1). The maximum surface density determined from ES-DMA for SH-PEG1K and SH-PEG5K shows close agreement with ATR-FTIR (i.e., $\sigma_{SH-PEG,max} \sim M_m^{-1.3}$). By contrast, the plateau level for $\sigma_{SH-PEG20K}$ as determined by ES-DMA is $\sim$6 times lower than the corresponding value determined by ATR-FTIR. One explanation for the substantial difference could be attributed to an
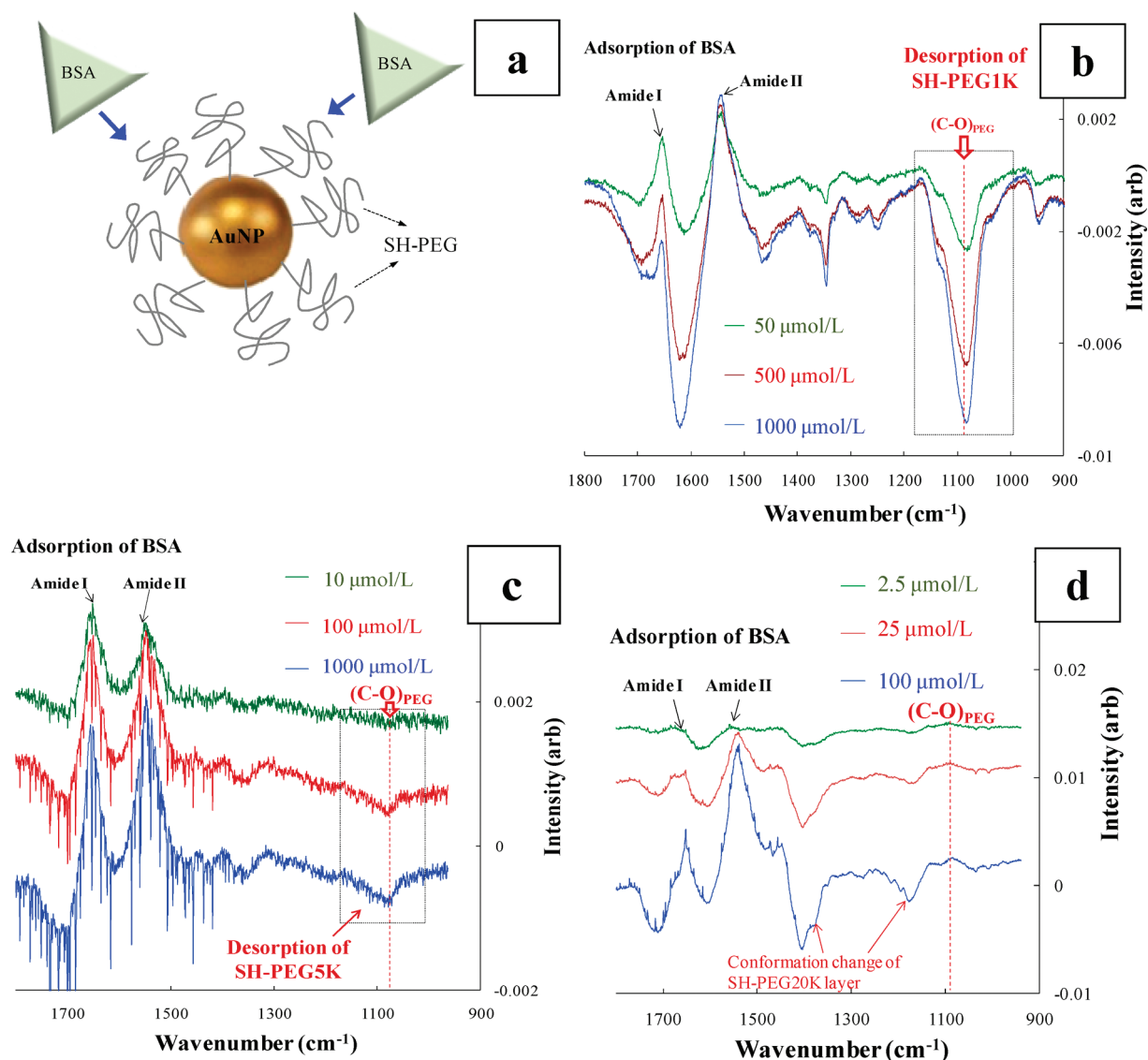
Figure 6. Ligand displacement on SH-PEG-conjugated AuNPs following introduction of BSA. (a) Cartoon depicting BSA interacting with SH-PEG-conjugated AuNPs. (b) IR difference spectra for BSA adsorption on SH-PEG1K-conjugated AuNPs. (c) IR difference spectra for BSA adsorption on SH-PEG5K-conjugated AuNPs. (d) IR difference spectra for BSA adsorption on SH-PEG20K-conjugated AuNPs.

overestimated cross-sectional surface area for the longer polymer chain (SH-PEG20K) as applied to the calculation of surface density, where it has been previously shown to yield up to about 5× lower values than results obtained by other methods for surface density evaluation.[14] Further discussion of this issue is provided in section 5 of the Supporting Information. Because of a good semiquantitative agreement, especially for SH-PEG1K and SH-PEG5K, we will continue to use ES-DMA as our orthogonal tool in the subsequent section.

As shown in Figure 4a,b, the adsorption isotherm curves follow a Langmuir-like behavior (i.e., chemisorbed monolayer). Using the Langmuir adsorption model, the equilibrium binding constant, K, is obtained:

$$\frac{\sigma_{max}}{\sigma} - 1 = \frac{1}{K}\frac{1}{C_m} \tag{5}$$

Figure 4c shows the Langmuir fits for three different SH-PEG measured by ATR-FTIR. K is estimated from the slope, $1/K$, and

shows that increasing M_m of SH-PEG increases the surface binding constants to AuNPs (summarized in Table 1). The results show that even though the adsorption of SH-PEG is principally via S−Au bonding, the polymer chain may still play a role in the adsorption process; with longer chain lengths (higher M_m) it is possible to have more contacts between the SH-PEG and the AuNP surface. Hence, K may be higher for larger M_m SH-PEG in accordance with the increase in chain length and nonspecific interactions with the AuNP surface. Figure 4d shows the Langmuir fits for the ES-DMA isotherm data. Similar to the results by ATR-FTIR (summarized in Table 1), K values for SH-PEG5K and SH-PEG20K were significantly higher than SH-PEG1K; the differences between SH-PEG5K and SH-PEG20K do not appear to be attributable to the fitting uncertainties.

d. Simultaneous Competitive Adsorption. In this section, we will demonstrate how results obtained from in-situ ATR-FTIR can be used to investigate simultaneous competitive adsorption (as pictured in a simplified cartoon, Figure 5a) and
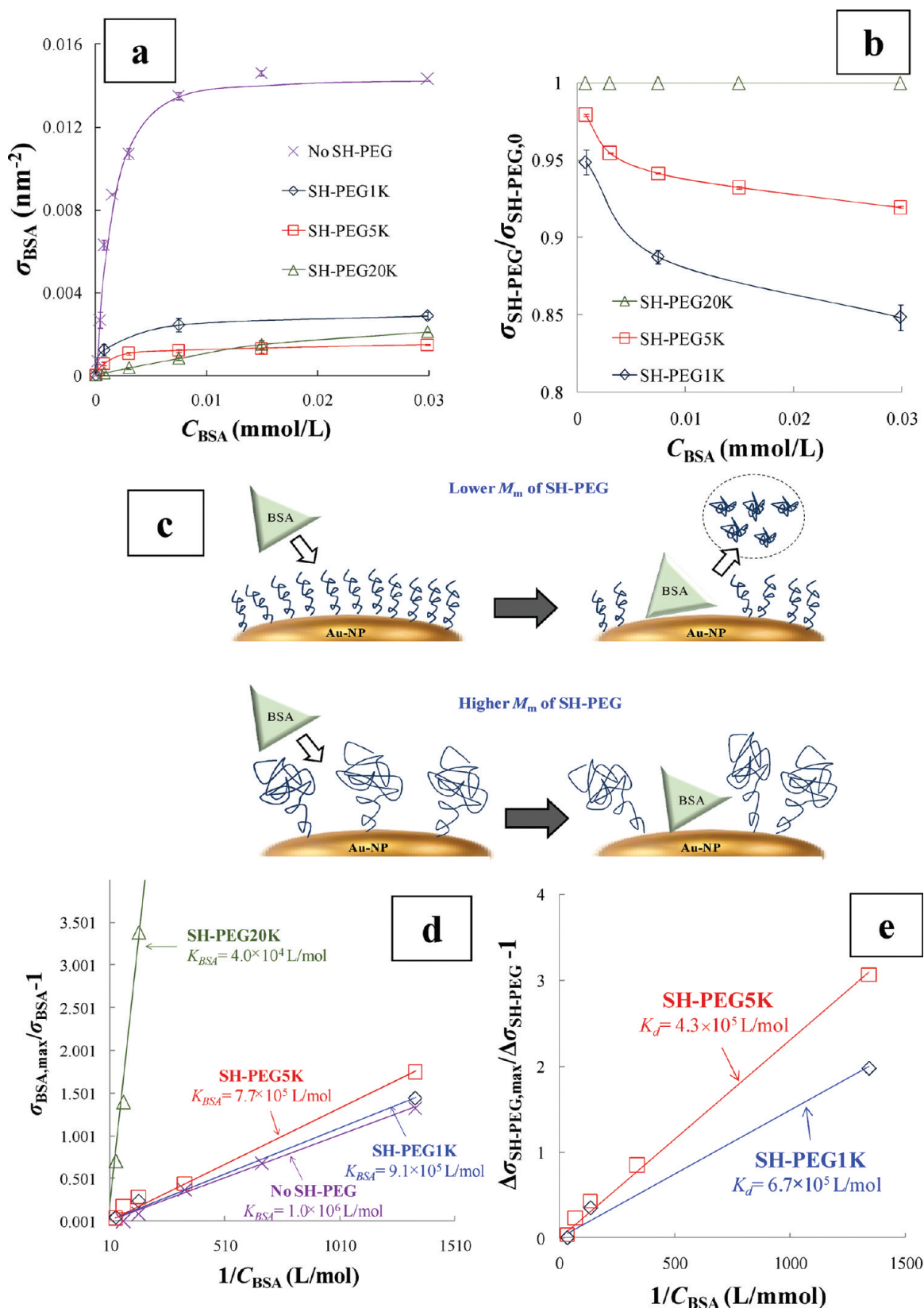
Figure 7. Analysis of ligand displacement for SH-PEG by BSA on SH-PEG-conjugated AuNPs, shown for three SH-PEG molecular mass values. (a) Adsorption isotherms for BSA; lines are to guide the eyes. (b) Desorption isotherms for SH-PEG in the presence of BSA; lines are to guide the eyes. (c) Cartoon depictions of ligand displacement by BSA. (d) Calculation of equilibrium binding constant for BSA, K_{BSA}, obtained from fits (solid lines) to the Langmuir adsorption model; the slope represents $1/K_{BSA}$. (e) Calculation of equilibrium desorption constant for SH-PEG, K_d, in the presence of BSA obtained from fit to the Langmuir model; the slope represents $1/K_d$.

Table 2. Summary of Ligand Displacement on SH-PEG-Conjugated AuNPs Following Introduction of BSA Measured by ATR-FTIR

species	σ_{BSA} (nm^{-2})	$\Delta\sigma_{SH\text{-}PEG}$ (nm^{-2})	K_{BSA} (L/mol)	K_d (L/mol)	R
SH-PEG1K	0.001−0.003	0.11−0.33	9.1×10^5	6.7×10^5	59.5 ± 20.1
SH-PEG5K	0.001−0.002	0.005−0.02	7.7×10^5	4.3×10^5	4.2 ± 2.7
SH-PEG20K	0.001−0.002	≈ 0	4×10^4	≈ 0	≈ 0

to benchmark ligand adsorption results based on particle size data obtained by ES-DMA. Figure 5b shows the IR spectra for a mixture of MPA and SH-PEG5K conjugates on AuNPs. The concentration of SH-PEG5K is fixed at 0.05 mmol/L, and the concentration of MPA (C_{MPA}) varies from 0 to 1.44 mmol/L. When C_{MPA} = 0 mmol/L, the strong absorbance at 1080 cm^{-1} (characteristic for SH-PEG5K) is clearly evident, while absorbance at 1240 cm^{-1} (characteristic for MPA) is clearly absent. Upon addition of C_{MPA}, the intensity of the $(C-O)_{MPA}$ band increases and is accompanied by a decrease in the $(C-O)_{PEG}$ band, indicating that the adsorption density for SH-PEG5K on the AuNP surface decreases due to competitive uptake of MPA.

Based on ATR-FTIR spectral analysis, calculated adsorption isotherms for SH-PEG on AuNPs are shown in Figure 5c; the adsorption plateau decreases significantly from 0.16 to 0.03 nm^{-2} as the MPA concentration increases from 0 to 1.44 mmol/L. A comparison with isotherms obtained from the analysis of ES-DMA particle size data (shown in Figure 5d) indicates consistency at a semiquantitative level, and together the two data sets demonstrate that MPA strongly inhibits the uptake of SH-PEG5K on AuNPs under conditions of simultaneous competitive adsorption.

In contrast to the physical measurement approaches, we have adapted to characterize the adsorption behavior of relatively large chain ligands, such as SH-PEG5K. ATR-FTIR is equally adroit at differentiating and quantifying the uptake of *small chain* molecules, such as MPA, even in the presence of the aforementioned large chain ligands. This differentiation is possible due to the specificity of IR absorption bands. For example, Figure 5e shows σ_{MPA} versus $C_{SH\text{-}PEG5K}$; compared with MPA adsorption in the total absence of SH-PEG, it is evident that the presence of SH-PEG leads to an initial decrease in $\sigma_{MPA,max}$ to about 26−42% of its noncompetitive adsorption value ($\sigma_{MPA,max} \approx 6.5$ nm^{-2}). A possible reason for the reduced MPA uptake is that the presence of SH-PEG5K induces steric hindrance. Because MPA occupies at least 10× more S−Au binding sites relative to SH-PEG5K at the highest $\sigma_{SH\text{-}PEG}$ value, σ_{MPA} decreases by less than 5% of the corresponding maximum values over the $C_{SH\text{-}PEG5K}$ range used in this study Hence, the presence of SH-PEG5K does in fact inhibit the adsorption of MPA, but that effect weakens significantly upon further increase in SH-PEG5K concentration. From a qualitative standpoint, MPA adsorption is more strongly dependent on C_{MPA} than $C_{SH\text{-}PEG5K}$.

e. Ligand Displacement Competitive Adsorption. In the present study, BSA was selected to represent the predominant serum protein as a potential displacing ligand for SH-PEG-conjugated AuNPs (simplistically illustrated by a cartoon in Figure 6a). Figure 6b−d shows the IR difference spectra obtained for SH-PEG conjugated AuNPs after BSA has been introduced to the system (experiments have been described in section 2b). Three M_m values for SH-PEG (SH-PEG1K, SH-PEG5K, and SH-PEG20K) were interrogated. For SH-PEG1K (Figure 6b) and SH-PEG5K (Figure 6c) conjugated AuNPs, we

observe strong negative absorbance for $(C-O)_{PEG}$ (≈ 1080 cm^{-1}) that varies with BSA concentration (C_{BSA}), indicating SH-PEG1K and SH-PEG5K are desorbed from the surface of AuNPs in the presence of BSA. At the same time, we observe two peaks, at 1540 and 1650 cm^{-1}, which are known as the amide II peak and amide I peak for BSA,[24,35] respectively. Formation of these two BSA peaks confirms the adsorption of BSA on the surface of SH-PEG1K- and SH-PEG5K-conjugated AuNPs. In the following analysis, we rely on the amide II band for quantifying the uptake of BSA due to less interference from the absorbance of water (≈ 1620 cm^{-1}) relative to the amide I band.[24] As C_{BSA} increases, both the negative absorbance of $(C-O)_{PEG}$ and the positive absorbance of the amide I peak (≈ 1540 cm^{-1}) increase.

By contrast, BSA adsorption on SH-PEG20K-conjugated AuNPs results in significant increases for peaks at 1540 and 1650 cm^{-1} as shown in Figure 6d, but without the concomitant change in the $(C-O)_{PEG}$ band observed for the lower molecular mass SH-PEG species; this suggests the adsorption of BSA does not induce significant desorption of SH-PEG20K (at least within the method's detection limit). The capacity for the higher molecular mass SH-PEG20K-conjugated AuNPs to adsorb BSA without displacing the PEG molecule may be in part due to the greater separation distance between the larger SH-PEG molecules and their ability to shift or alter their conformation to accommodate BSA adsorption. The average separation distance between SH-PEG20K on AuNPs is ≈ 4.5 nm, much greater than that associated with SH-PEG1K (≈ 0.8 nm) and almost twice that of SH-PEG5K (2.5 nm), yet sufficient to accommodate the minimum dimension ("depth"; modeled as a three-dimensional equilateral triangle) of heart-shaped N-type (normal form) BSA (≈ 3 nm).[36,37] Evidence to support this hypothesis is found in the appearance of negative peaks at 1160 and 1400 cm^{-1}, as shown in Figure 6d. The negative absorbance at these bands is suggestive of a molecular conformational change in the adsorbed SH-PEG (details in section 3 of the Supporting Information), the result of which is accommodation of BSA molecules without actual displacement of SH-PEG20K from occupied sites.

Figure 7 summarizes results obtained from an analysis of ATR-FTIR spectra for ligand displacement shown in Figure 6; BSA adsorption and SH-PEG desorption are plotted against C_{BSA}. Increasing C_{BSA} from 0.75 to 29.8 μmol/L increases the surface density of BSA, σ_{BSA} (summarized in Table 2). In addition, the maximum σ_{BSA} on SH-PEG conjugated AuNPs is in the range 18−32% relative to σ_{BSA} determined on native (citrate-stabilized) AuNPs (0.014 nm^{-2}), demonstrating that SH-PEG inhibits the binding of BSA on AuNPs over the range of SH-PEG molecular mass values considered in the present study; notably, this inhibition increases with M_m, indicating perhaps a stronger steric hindrance by higher M_m SH-PEG.

At the same time, as shown in Figure 7b, $\sigma_{SH\text{-}PEG}$ decreases with C_{BSA} for SH-PEG1K and SH-PEG5K but is unchanging for SH-PEG20K when C_{BSA} increases from 0.75 to 29.8 μmol/L (summarized in Table 2, $\Delta\sigma_{SH\text{-}PEG} = \sigma_{SH\text{-}PEG,0} - \sigma_{SH\text{-}PEG}$, where

$\sigma_{\text{SH-PEG},0}$ is the initial $\sigma_{\text{SH-PEG}}$ before BSA interaction). The results quantitatively confirm that SH-PEG-AuNP conjugate stability in the presence of serum albumin improves as M_{m} increases. A cartoon of the ligand displacement reaction is shown in Figure 7c based on the results in Figure 7a,b.

To quantify the effect of ligand displacement, we define a ratio, R

$$R = \frac{\Delta\sigma_{\text{SH-PEG}}}{\sigma_{BSA}} \qquad (6)$$

Higher R values indicate more SH-PEG was removed due to the adsorption of BSA. As shown in Table 2, R is inversely proportional to M_{m} of SH-PEG.

The Langmuir adsorption model is used to quantify the affinities of BSA adsorption onto, as well as SH-PEG desorption from, the surface of SH-PEG conjugated AuNPs. Figure 7d shows fits to the linear form of the Langmuir model for BSA adsorption, where the slope is $1/K_{\text{BSA}}$ (K_{BSA} values are summarized in Table 2). By comparison, K_{BSA} obtained for BSA adsorption onto native (citrate-stabilized) AuNPs is substantially higher (1.0×10^6 L/mol). The results confirm that BSA binding affinity is reduced when SH-PEG is present on the AuNP surface and show that this suppression increases with SH-PEG molecular mass.

The Langmuir model can be applied to quantify the desorption (displacement) behavior of SH-PEG in the presence of BSA as follows:

$$\frac{\Delta\sigma_{\text{SH-PEG},max}}{\Delta\sigma_{\text{SH-PEG}}} - 1 = \frac{1}{K_{\text{d}}C_{BSA}} \qquad (7)$$

Here $\Delta\sigma_{\text{SH-PEG,max}}$ is the maximum $\Delta\sigma_{\text{SH-PEG}}$, and K_{d} is the desorption constant for SH-PEG after BSA interaction. From the slope ($1/K_{\text{d}}$) shown in Figure 7e, K_{d} is 6.7×10^5 L/mol for SH-PEG1K, 4.3×10^5 L/mol for SH-PEG5K, and not measurable for SH-PEG20K. These results further confirm that the ability of SH-PEG to resist displacement by serum albumin increases with molecular mass, a fact that is clearly relevant for the formulation of nanoparticle-based vectors for therapeutic applications.

4. SUMMARY AND CONCLUSIONS

In this study, ATR-FTIR spectroscopy has been successfully adapted to characterize molecular conjugation on AuNPs, both qualitatively and semiquantitatively, within the context of nanomedicine formulation. Adsorption isotherms for SH-PEG at three molecular mass values (1, 5, and 20 kDa) indicate that the adsorption density, $\sigma_{\text{SH-PEG}}$, is inversely proportional to the molecular mass. Adsorption isotherms obtained by ES-DMA are employed for an orthogonal comparison, and both the surface density and the equilibrium binding constants obtained for SH-PEG reflect good agreement between ES-DMA and ATR-FTIR at the semiquantitative level.

The ATR-FTIR approach developed herein was applied to study competitive adsorption, in which more than one ligand is present; competitive adsorption is relevant to biomedical applications where multiple functionalities are typically required and where introduction into a biological matrix may result in displacement of functional surface groups by thiol-presenting serum proteins. Under conditions of simultaneous competition, results show that increasing the concentration of MPA reduces the surface density and binding affinity of SH-PEG. By contrast, even though SH-PEG5K does in fact inhibit the initial adsorption of MPA, that effect weakens upon further increase in SH-PEG5K concentration, suggesting that the SH-PEG-conjugated surface is able to accommodate the small molecule MPA due to single-thiol binding of the much larger and flexible SH-PEG molecules; this behavior is dependent on the molecular mass of SH-PEG, with larger PEG molecules being more accommodating with respect to MPA. Under conditions of ligand displacement competition, the binding affinity of the displacer, BSA, is reduced on PEG-functionalized AuNPs relative to adsorption on the native AuNPs; affinity decreases as the molecular mass of SH-PEG increases. It is demonstrated that the modified ATR-FTIR method presented in this study can be applied to study competitive adsorption between any combinations of molecular adsorbates, so long as distinct ligand-specific IR bands can be identified and exploited.

Future work will seek to extend this method to more complex multifunctional AuNP-based cancer therapeutics that include targeting, imaging, and other modalities as well as more realistic models of biological matrices that combine, for instance, antibodies, sugars, and serum proteins. Through an in-situ semiquantitative analysis of particle−molecule interactions, as demonstrated in this study, parameters such as equilibrium binding and desorption constants can be obtained and then used to improve the formulation design and quality assurance for nanomedicine constructs. The work presented here provides proof of concept and demonstrates the efficacy of the ATR-FTIR approach for the effective investigation of molecular conjugation in AuNP systems.

■ ASSOCIATED CONTENT

ⓢ Supporting Information. Additional information. This material is available free of charge via the Internet at http://pubs.acs.org.

■ AUTHOR INFORMATION

Corresponding Author
*E-mail: vincent.hackley@nist.gov.

■ ACKNOWLEDGMENT

■ REFERENCES

(1) Borm, P.; Robbins, D.; Haubold, S.; Kuhlbusch, T.; Fissan, H.; Donaldson, K.; Schins, R.; Stone, V.; Kreyling, W.; Lademann, J.; Krutmann, J.; Warheit, D.; Oberdorster, E. *Part. Fibre Toxicol.* **2006**, 3:11.

(2) Dobrovolskaia, M. A.; Mcneil, S. E. *Nature Nanotechnol.* **2007**, 2 (8), 469–478.

(3) Domingos, R. F.; Tufenkji, N.; Wilkinson, K. J. *Environ. Sci. Technol.* **2009**, 43 (5), 1282–1286.

(4) Yang, J.; Zeng, J.; Kong, T.; Wang, X.; Roa, W.; El-Bialy, T.; Xing, J.; Chen, J. 2007 IEEE/NIH Life Science Systems and Applications Workshop. DOI 10.1109/LSSA.2007.4400892, 2007.

(5) Karakoti, A. S.; Hench, L. L.; Seal, S. *JOM* **2006**, 58 (7), 77–82.

(6) Li, S. D.; Huang, L. *Mol. Pharmaceutics* **2008**, 5 (4), 496–504.

(7) Oberdörster, J.; Maynard, A.; Donaldson, K.; Castranova, V.; Fitzpatrick, J.; Ausman, K.; Carter, J.; Kreyling, W.; Karn, B.; Lai, D.;

Olin, S.; Monteiro-Riviere, N.; Warheit, D.; Yang, H. *Part. Fibre Toxicol.* **2005**, 2:8.

(8) Walczyk, D.; Bombelli, F. B.; Monopoli, M. P.; Lynch, I.; Dawson, K. A. *J. Am. Chem. Soc.* **2010**, *132* (16), 5761–5768.

(9) Corrigan, T. D.; Guo, S.; Phaneuf, R. J.; Szmacinski, H. *J. Fluoresc.* **2005**, *15* (5), 777–784.

(10) Corrigan, T. D.; Guo, S. H.; Szmacinski, H.; Phaneuf, R. J. *Appl. Phys. Lett.* **2006**, *88*, 10.

(11) Dobrovolskaia, M. A.; Patri, A. K.; Zheng, J. W.; Clogston, J. D.; Ayub, N.; Aggarwal, P.; Neun, B. W.; Hall, J. B.; Mcneil, S. E. *Nanomed.-Nanotechnol. Biol. Med.* **2009**, *5* (2), 106–117.

(12) Guo, S. H.; Tsai, S. J.; Kan, H. C.; Tsai, D. H.; Zachariah, M. R.; Phaneuf, R. J. *Adv. Mater.* **2008**, *20* (8), 1424.

(13) Lacerda, S. H. D.; Park, J. J.; Meuse, C.; Pristinski, D.; Becker, M. L.; Karim, A.; Douglas, J. F. *ACS Nano* **2010**, *4* (1), 365–379.

(14) Pease, L. F.; Tsai, D. H.; Zangmeister, R. A.; Zachariah, M. R.; Tarlov, M. J. *J. Phys. Chem. C* **2007**, *111* (46), 17155–17157.

(15) Pease, L. F.; Lipin, D. I.; Tsai, D. H.; Zachariah, M. R.; Lua, L. H. L.; Tarlov, M. J.; Middelberg, A. P. J. *Biotechnol. Bioeng.* **2009**, *102* (3), 845–855.

(16) Tsai, D. H.; Zangmeister, R. A.; Pease, L. F.; Tarlov, M. J.; Zachariah, M. R. *Langmuir* **2008**, *24* (16), 8483–8490.

(17) Tsai, D. H.; Delrio, F. W.; MacCuspie, R. I.; Cho, T. J.; Zachariah, M. R.; Hackley, V. A. *Langmuir* **2010**, *26* (12), 10325–10333.

(18) Paciotti, G. F.; Myer, L.; Weinreich, D.; Goia, D.; Pavel, N.; McLaughlin, R. E.; Tamarkin, L. *Drug Delivery* **2004**, *11* (3), 169–183.

(19) Tsai, D. H.; Pease, L. F.; Zangmeister, R. A.; Tarlov, M. J.; Zachariah, M. R. *Langmuir* **2009**, *25* (1), 140–146.

(20) Tamarkin, L. FDA/ANH Critical Path Nanotechnology Workshop, Houston, TX, 2008.

(21) Koo, O.; Rubinstein, I.; Onyuksel, H. *Nanomedicine* **2005**, *1* (3), 193–212.

(22) Myshko, D. *PharmaVoice* **2004**, February, 1–6.

(23) U.S. Department of Health and Human Services National Institutes of Health National Cancer Institute http://nano.cancer.gov/objects/pdfs/Cancer_brochure_091609-508.pdf, 2004.

(24) Tsai, D. H.; Delrio, F. W.; Keene, A. M.; Tyner, K. M.; MacCuspie, R. I.; Cho, T. J.; Zachariah, M. R.; Hackley, V. A. *Langmuir* **2011**, *27* (6), 2464–2477.

(25) Lin, W. D.; Li, Z. J. *Anal. Chem.* **2010**, *82* (2), 505–515.

(26) Tejedor-Tejedor, M. I.; Paredes, L.; Anderson, M. A. *Chem. Mater.* **1998**, *10* (11), 3410–3421.

(27) Tickanen, L. D.; Tejedor-Tejedor, M. I.; Anderson, M. A. *Langmuir* **1997**, *13* (18), 4829–4836.

(28) Dobson, K. D.; Connor, P. A.; McQuillan, A. J. *Langmuir* **1997**, *13* (10), 2614–2616.

(29) Dobson, K. D.; Roddick-Lanzilotta, A. D.; McQuillan, A. J. *Vib. Spectrosc.* **2000**, *24* (2), 287–295.

(30) Certain commercial equipment, instruments, or materials are identified in this report in order to specify the experimental procedure adequately. Such identification is not intended to imply recommendation or endorsement by the National Institute of Standards and Technology, nor is it intended to imply that the materials or equipment identified are necessarily the best available for the purpose.

(31) Winn, J. S. *Physical Chemistry*; Harper Collins: New York, 1994.

(32) Socrates, G. *Infrared Characteristic Group Frequencies*; John Wiley and Sons: New York, 1994.

(33) Sandhyarani, N.; Pradeep, T. *Int. Rev. Phys. Chem.* **2003**, *22* (2), 221–262.

(34) Netz, R. R.; Andelman, D. *Phys. Rep.* **2003**, *380* (1−2), 1–95.

(35) Roach, P.; Farrar, D.; Perry, C. C. *J. Am. Chem. Soc.* **2005**, *127* (22), 8168–8173.

(36) Carter, D. C.; Ho, J. X. *Adv. Protein Chem.* **1994**, *45*, 153–203.

(37) Ferrer, M. L.; Duchowicz, R.; Carrasco, B.; de la Torre, J. G.; Acuna, A. U. *Biophys. J.* **2001**, *80* (5), 2422–2430.